

Article

# Formation Mechanism of Deposits in Rotary Kiln during Steelmaking Dust Carbothermic Recycling

Xiaobo Min<sup>1,2,3</sup>, Luyu Huang<sup>1</sup>, Maixin Yu<sup>1</sup>, Yunyan Wang<sup>1,2,3</sup>, Yong Ke<sup>1,2,3</sup>, Cong Peng<sup>1,2,3</sup> , Xu Yan<sup>1,2,3</sup>, Qingyu Huang<sup>1</sup> and Yun Li<sup>1,2,3,\*</sup>

<sup>1</sup> School of Metallurgy and Environment, Central South University, Changsha 410083, China; mxbcusu@163.com (X.M.); 213511059@csu.edu.cn (L.H.); ymaixia@126.com (M.Y.); wyy@csu.edu.cn (Y.W.); keyong000ke@csu.edu.cn (Y.K.); pengcong0704@csu.edu.cn (C.P.); yanxu1202@csu.edu.cn (X.Y.); qingyuhuang@csu.edu.cn (Q.H.)

<sup>2</sup> State Key Laboratory of Advanced Metallurgy for Non-Ferrous Metals, Central South University, Changsha 410083, China

<sup>3</sup> Chinese National Engineering Research Center for Control & Treatment of Heavy Metal Pollution, Central South University, Changsha 410083, China

\* Correspondence: li.yun@csu.edu.cn

**Abstract:** Rotary kiln has been widely used in hazardous waste treatment because of its strong adaptability to raw materials, high productivity, and simple processing technology. However, the formation of deposits reduces its performance period and profitability. This study characterized the deposit mineralogy and thermodynamically and experimentally investigated its formation mechanism. The results show that the main phases of the deposit are magnetite, monolithic iron, olivine, and yellow feldspar. They indicate that the deposit formation process was accompanied by the participation of alkaline and iron oxides. The intermediate product  $\text{Ca}_2\text{SiO}_4$  can promote the generation of low melting point phases, such as  $\text{CaFeSiO}_4$  and  $\text{Ca}_2\text{Al}_2\text{SiO}_7$ , which are the main phases of deposit materials. Additionally, the reduction intermediate product FeO facilitated the generation of a liquid ferrous mixture ( $\text{Fe}_3\text{O}_4$ -FeO and  $\text{Fe}_3\text{O}_4$ -FeO-Fe mixture), which in turn further promoted the growth of the initial deposit phase. The solid deposit formed and attached to the kiln inner wall, along with a decrease in temperature. These results are expected to provide an idea or approach for fundamentally solving the problem of deposits in the rotary kiln.



**Citation:** Min, X.; Huang, L.; Yu, M.; Wang, Y.; Ke, Y.; Peng, C.; Yan, X.; Huang, Q.; Li, Y. Formation Mechanism of Deposits in Rotary Kiln during Steelmaking Dust

Carbothermic Recycling. *Separations* **2024**, *11*, 137. <https://doi.org/10.3390/separations11050137>

Received: 28 March 2024

Revised: 17 April 2024

Accepted: 27 April 2024

Published: 29 April 2024



**Copyright:** © 2024 by the authors. Licensee MDPI, Basel, Switzerland. This article is an open access article distributed under the terms and conditions of the Creative Commons Attribution (CC BY) license (<https://creativecommons.org/licenses/by/4.0/>).

**Keywords:** steelmaking dust; rotary kiln; deposit; zinc recovery; formation mechanism

## 1. Introduction

The iron and steel industry plays an indispensable role in the development of economic construction worldwide, especially in China, which has been the world's largest lead producer and consumer for several years [1]. However, it produces a huge output of steelmaking dusts [2]. In addition to a large number of iron elements, zinc, manganese, nickel, copper, sodium, gold, silver, and other valuable metal elements are contained in these dusts [3]. At the same time, the steelmaking dust is enriched with a certain number of indium, bismuth, tin, cadmium, and other rare elements with high added value, which are valuable resources. Therefore, sometimes these dusts are also a good sintering raw material [4]. World steel statistics show that, in 2022, the world crude steel production was 1.885 billion tons, and China crude steel production was 1.018 billion tons.

It is reported that every ton of steel production generates around 100 kg of iron-containing dust or mud. In China, the annual production of steelmaking dust and mud is more than 100 million tons. If not recycled, it will not only cause a great waste of resources, but also seriously pollute the environment [5,6]. Considering the more and more severe situation of energy, resources, and environment, the pressure of iron and steel enterprises is increasingly huge. Resource utilization of steelmaking dusts not only meets

the requirements of environmental protection policies, but also generates considerable economic benefits [7]. Therefore, it is urgent to solve the problem of the efficient recycling of steelmaking dust and mud.

Rotary kilns are widely used in the metallurgical industry and is one of the main industrial methods used to process steelmaking dust and mud [8,9]. The furnace body is a long cylinder with a certain dip angle. During rotation, the material is slowly fed into the furnace along the dip angle [10]. The material is turned along the circumference while moving along the axial direction, so that it flows slowly through the whole cylinder, undergoing complex physicochemical changes and completing the reaction process. Then, it is discharged from the end of the kiln into the cooling system [11]. This process has the advantages of low capital investment, strong adaptability, large production capacity, and flexible operation [12–14]. The iron oxides in the dust are reduced to metallic iron or low-valence iron oxide; at the same time, the zinc oxides are reduced to metallic zinc under high-temperature conditions in the rotary kiln using carbon as the fuel. The zinc is gasified at a high temperature into the flue gas and then oxidized again to become secondary zinc oxide powder. The flue gas is discharged from the end of the rotary kiln, followed by cooling down, and is then collected by a bag filter to collect the zinc oxide powder. The reduced iron-rich slag is discharged from the rotary kiln head and then water is cooled to use as the sintering raw material [15–17]. However, during the high-temperature operation, materials in the rotary kiln often attach to the kiln wall after a series of physical and chemical reactions. The attachment moves along with the rotary kiln rotating, and then grows continuously to form the deposit.

The formation of rotary kiln deposit wastes raw materials and fuel, and makes the process system abnormal and out of control [18]. If the deposits grow thick enough, the kiln must be stopped and the deposits removed, resulting in a decrease in production efficiency and a great increase in costs [19,20]. Deposit formation has been attributed to unstable operating conditions, fuel and ash properties, combustion conditions, feed material properties, accumulation phenomenon, and chemical reactions [21,22]. Early researchers hoped to solve these problems by continually studying raw material properties, chemical additives, and physical removal techniques [23,24]. These have achieved some results, but cannot fundamentally solve the problems. In order to control the growth of deposits, it is necessary to study the growth behavior and formation mechanism of the deposit.

Recently, many scholars have carried out extensive research on the deposits that form in the rotary kiln, and put forward some preventive measures. Zhong et al. [25] investigated the effect of coal ash on the performance of ball powder rings in kilns. Results showed that coal ash not only changed the chemical composition of pellet powder, but also influenced its bonding process. Hou et al. [26,27] studied the influence of the ash performance and combustibility of the coal on ring growth behaviors within a pellet's kiln, proposing that coal ashes with good soft fusibility and weak bonding were less likely to form low melting point substances and, thus, form deposits. In addition, Luo et al. [28] found that the presence of the elements Na, K, and F increased the liquid phase in the mixture and promoted the formation of deposits in the kiln.

Some researchers have focused on the effect of reactions occurring in the rotary kiln on deposit formation. Zhong et al. [29] studied the characteristics and formation mechanism of spheroidized sphericity in rotary kiln smelting of low-grade iron ore, and found that low melting point phases, such as iron olivine and calcium pyroxene, were the main causes of deposit formation. Researchers Si et al. [30] studied the mineral phase structure of deposits in the pellet's rotary kiln. They considered that the formation mechanism of deposits were predominantly attributed to the solid phase consolidation of iron oxide and liquid phase agglomeration of low melting point substances. These results are consistent with that of investigations conducted by Yang et al. [31].

Some other scholars focused not only on the feedstock and reaction, but also on the effect of reaction conditions on deposits. Fan et al. [32] found that a high temperature

in the kiln, substances with low melting point, and a large content of ultrafine powder were important influencing factors of deposit formation in the middle of the rotary kiln, and long residence time of powder at the end of the kiln was the main reason for deposit formation at the end of the kiln. Nie et al. [33] considered that excessive coal ash after burning in the rotary kiln and excessive baking temperature were the two main reasons for deposit formation in the kiln. Wang et al. [34] studied the layered structure and formation mechanism of deposits forming material in the pre-reduction rotary kiln and found that the ring forming material can be divided into a dense layer and loose layer. They believe that the instability of roasting temperatures and the formation of low melting point matter are the main factors of deposits forming in the rotary kiln.

Although deposit formation in rotary kiln applications has been studied, considering the complex formation reasons caused by variable feeding materials and different operation conditions, this investigation is still not enough. Deposits are one of the main factors affecting the continuous and stable operation of the rotary kiln, as well as economic and technical indicators. Therefore, it is necessary to study the formation path and to further know its inhibition method. In this paper, the circle-forming material produced in the actual rotary kiln process of handling steelmaking dust and mud was studied. The formation mechanism was understood thermodynamically and experimentally in terms of the properties of the ring-forming material. The composition and surface microstructure composition of deposit samples were analyzed by X-ray fluorescence (XRF) and scanning electron microscope-energy dispersion spectroscopy (SEM-EDS). The distribution pattern of the main elements in the deposits was investigated by an automatic mineral parameter analyzer (MLA). Moreover, X-ray diffraction (XRD) was used to analyze the crystal phases formed in the ring. In addition, the influence of FeO and Fe<sub>3</sub>O<sub>4</sub> on the deposit formation and evolution mechanism were investigated through a series of experiments. Finally, on the basis of theoretical analysis and experimental research, a possible deposit formation mechanism in the rotary kiln was proposed, which is expected to provide a new insight into the suppression of ring formation.

## 2. Materials and Methods

### 2.1. Experimental Materials

The raw deposit material was supplied by a steel plant in China, which handles 500 tons of steelmaking dusts (including blast furnace electrostatic precipitator dust, electric furnace ash, and converter dust) per day. The roasting takes place in the combustion chamber in the rotary kiln ( $\Phi 4 \times 60$  m). Figure 1a shows the longitudinal section of the deposit ring in the rotary kiln. The height of accumulated coils may affect the flow of raw materials and flue gas. The deterioration of the process conditions will lead to significant temperature changes in the pre-deposit area and the post-deposit area.

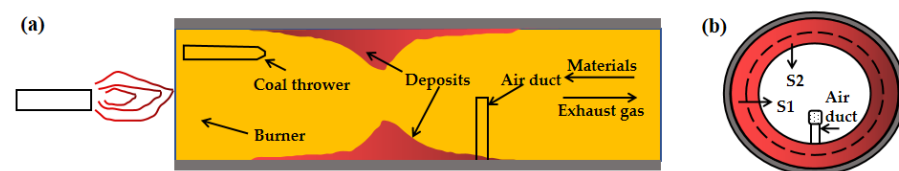


**Figure 1.** (a) Cross-sectional diagram of the rotary kiln furnace; (b) schematic diagram of sampling locations of different deposits.

To reveal the formation and growth mechanisms of deposits, two samples from different locations were obtained when the kiln was stopped for maintenance. The collection position on the cross section of the deposits on the kiln wall is shown in Figure 1b. The samples collected from the upper layer of the longitudinal section of the deposits were named as S1, which was the initial deposit-forming compound. Samples collected under the kiln wall were named as S2, which can be considered as the growth layer.

## 2.2. Experimental Methods

In order to investigate the characteristics and formation mechanism of the deposits, the physicochemical properties of the deposit materials were analyzed firstly. Then, thermodynamics were used to simulate the possible deposit formation process. Finally, experiments were designed and conducted to validate the accuracy of the assumed mechanism. During the experiment, the samples were finely ground using a three-head agate grinder. Then, the fine-grinded samples were pressed into a 10 mm cylinder using a tablet press, and roasted in a horizontal furnace at a desired temperature to simulate the actual rotary kiln roasting conditions. The baked samples were quenched in liquid nitrogen, ground fine, and tested for analyzing the influence of the deposit component formation mechanism. The experimental flow is schematically shown in Figure 2.

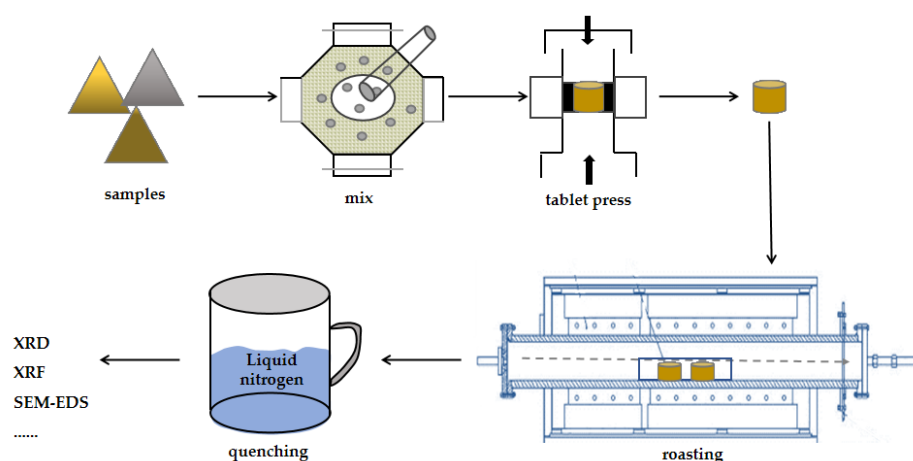


**Figure 2.** Schematic diagram of the experimental flow.

The chemical composition of the raw deposits and experimental samples obtained were determined by XRF (X-ray fluorescence, Axios mAX, PANalytical, Almelo, the Netherlands) and by Inductively Coupled Plasma-Optical Emission Spectrometer (ICP-OES, SPECTRO BLUE SOP, Spectrum Analytical Instruments, Kleve, Germany). XRF was tested by pressing the powdered samples using boric acid. The wavelength dispersive XRF was used in this experiment; and the x-ray tube anode was tungsten. Powder X-ray diffraction (XRD, D8 Advance, Cu-K $\alpha$ -radiation,  $\lambda = 1.54\text{\AA}$ , Bruker AXS Ltd., Karlsruhe, Germany) was performed on pulverized deposit samples to investigate physical phases with a Cu K $\alpha$  radiation. The data were collected in a  $2\theta$  range of  $10\text{--}80^\circ$ , with a  $2\theta$  step size of  $0.1^\circ$ . The semi-qualitative results were obtained by comparing the structure of samples with the data in the ICDD Powder Diffraction File database. A scanning electron microscopy coupled with an energy dispersive spectra analyzer (SEM-EDS, TESCAN MIRA LMS, Brno, Czech Republic) was employed to investigate the microscopic embedding morphology and elemental distributions of samples. Backscattered electrons (BSEs) were used to image for atomic number contrast. Elemental compositions were displayed as atom percent on a carbon-free and oxygen-free basis. Thermodynamic equilibrium simulations were conducted by FactSage 8.1 and its FToxide and FactPS database to predict the formation and inhibition path of deposits. Thermogravimetric-Differential Scanning Calorimetry (TG-DSC, NETZSCH STA 449F3, NETZSCH, Hanau, German) was combined to investigate the melting temperatures of samples.

## 3. Results and Discussion

### 3.1. Morphology and Chemical Composition of Deposits

The shape of the crystalline deposits was irregular. Figure 3 shows a cross-sectional view of the kiln deposit loop. It was observed that the deposit loop had a laminar structure. Near the kiln wall was the inner layer of the initial knotted material with loose texture

and low strength, which is mainly formed by the bond of eroded furnace refractory and the initial knotted material. The outer layer of the knotted material had a dense structure with a lot of bonded black and russet material, which was the main compound of the knotted material. A clear metallic luster (iron grey) deposit material and many molten substances connected to a piece indicated that there may have been metallic iron or iron oxides generated and melted together in the rotary kiln.

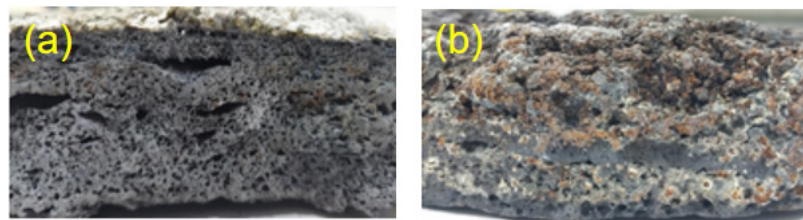


**Figure 3.** Morphological photos of deposit samples collected from different locations in the rotary kiln: (a) characteristics of the longitudinal section of S1; (b) characteristics of the longitudinal section of S2.

The chemical compositions of deposit samples S1 and S2 are listed in Table 1. The remaining chemical composition of the deposit is a small amount of impurities. The total iron content (TFe) of the deposits in the rotary kiln was more than 40%. The content of Ca and Si were relatively high, followed by Al and Mg, which may have been introduced from the refractory brick.

**Table 1.** Chemical compositions of deposit samples (wt%).

No.	TFe	O	Ca	Mg	Si	Al	Na	Mn
S1	40.16	30.22	13.94	2.48	4.98	4.06	0.39	0.77
S2	50.68	28.79	7.87	2.28	4.40	3.05	0.45	0.48

The remaining chemical composition of the deposit is a small amount of impurities.

The elements Fe, Ca, Si, and Al co-exist in the deposits and are able to form many different stable molten or solid–molten phases under the high temperature conditions in the rotary kiln.

### 3.2. Crystal Phase Composition of Deposits

The mineral phase of deposit samples S1 and S2 were determined by X-ray diffraction. The results are shown in Figure 4. The phase compositions of the two deposit samples comprised ferrous oxide, iron, magnetite, and silicate phases. By comparing the peak intensities of S1 and S2, the outer deposition (S2) contained more iron and less ferrous oxide than S1. This phenomenon may have been caused by different reducing environments. For internal S1, the reduction reaction of iron oxides took place in the initial reaction period and would be covered by the newly formed sediment. This stopped the further reduction of the iron oxides. For the outer deposit S2, as it was close to the flame, a higher temperature and longer reduction time may have led to a further reduction of the iron oxide, resulting in a higher content of low valence iron.

Combining the analysis of XRD and XRF results, the results indicate that Si and Ca were mainly in the form of silicate liquid phases in the deposit formation, and became the binding phase of the deposit formation. Iron-containing phases in the nodules were Fe, FeO, and Fe<sub>3</sub>O<sub>4</sub>. Elemental Al mainly existed in the form of low melting point, calcium–aluminium yellow feldspar in the deposit. The phases containing Mg, K, and Na were not shown in the XRD patterns. The presence of these small amounts of alkali metal elements in the material promotes the formation of low melting point compounds. They make the granular and powder materials stick more closely and make them difficult to remove. Some

scholars have shown that deposits in the rotary kiln are characterized by large amounts of Na, Si, Cl, Ca, and Fe. Its molten phase is mainly formed by alkali metal salts with low melting points, such as sodium chloride (801 °C) [12,35]. Zhu et al. [36] found that the main chemical compositions of the hazardous waste incineration residue were  $\text{SiO}_2$ ,  $\text{Al}_2\text{O}_3$ ,  $\text{Fe}_2\text{O}_3$ ,  $\text{CaO}$ , and  $\text{MgO}$ . As can be seen, rotary kilns react differently to different substances in the kiln. The composition of the final deposit material is also different.

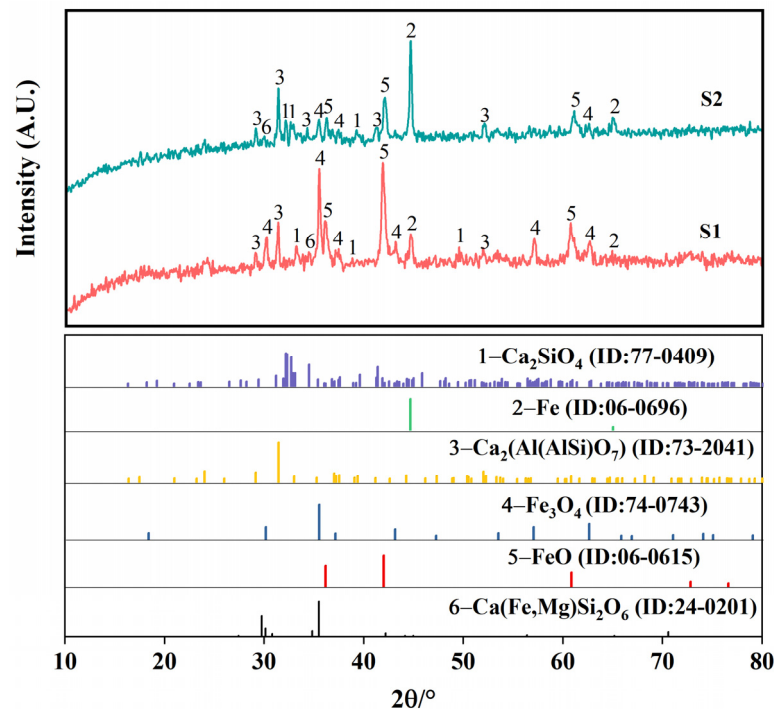


**Figure 4.** X-ray diffraction (XRD) patterns of deposits S1 and S2.

### 3.3. Microstructural Characterization of Deposits

The microstructure and phase composition of the actual deposit sample were analyzed using SEM-EDS techniques. The deposit sample was mounted by epoxy resin and then polished to a smooth mirror surface. The polished sample was coated with gold powder to reduce charge-build-up. The SEM-EDS analysis was conducted under a high-vacuum condition, with an accelerating voltage of 15 KV [37]. Figures 5 and 6 illustrate the SEM micrographs and EDS analysis of the deposit samples. Combining Figure 5 with the XRD results, Fe,  $\text{Fe}_3\text{O}_4$ , and Ca-Al-Si-O compounds existed in the position of S1, while sample S2 contained Fe, FeOx, and Ca-Al-Si-O compounds, as shown in Figure 6. S1 had more pores while S2 had almost no pores, indicating that S1 was not as dense as S2. Elemental iron particles varied greatly from S1 to S2. Embedded around metallic iron or iron oxides were silicate compounds, such as melilite and olivine. They were solidly dissolved together, and the low melting point phase became the main phase of the deposits.

According to the above analysis, a possible cooling and crystallization process of the deposits can be derived. It implied that in the initial formation stage, the main phases were the reduction products ferric oxide and  $\text{Ca}_2\text{SiO}_4$ . The good solid solubility of  $\text{Ca}_2\text{SiO}_4$  promoted the generation of low melting point phases, such as  $\text{Ca}_2\text{Al}_2\text{Si}_2\text{O}_7$ . With the continuous action of ambient temperature and reducing atmosphere, the deposits continued to accumulate and iron oxides continued to be reduced. Continuous burning in the kiln resulted in the reduction of hematite to magnetite ( $\text{Fe}_3\text{O}_4$ ) and wustite (FeO) [38]. Gradually, FeO appeared, and the  $\text{Fe}_3\text{O}_4$ -FeO mixture formed. FeO facilitated the generation of liquid slag, which in turn promoted the formation of the deposit phase. Eventually, a large number of metallic Fe was generated, making the ring junctions become dense and hard.

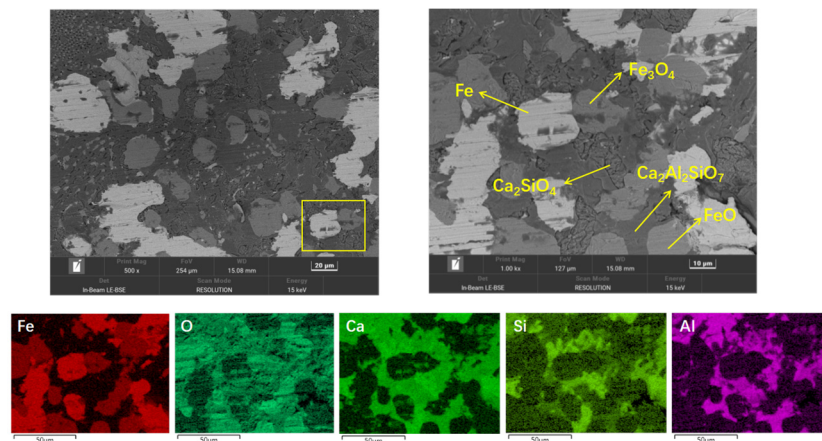


Figure 5. SEM-EDS analysis of internal deposit sample S1.

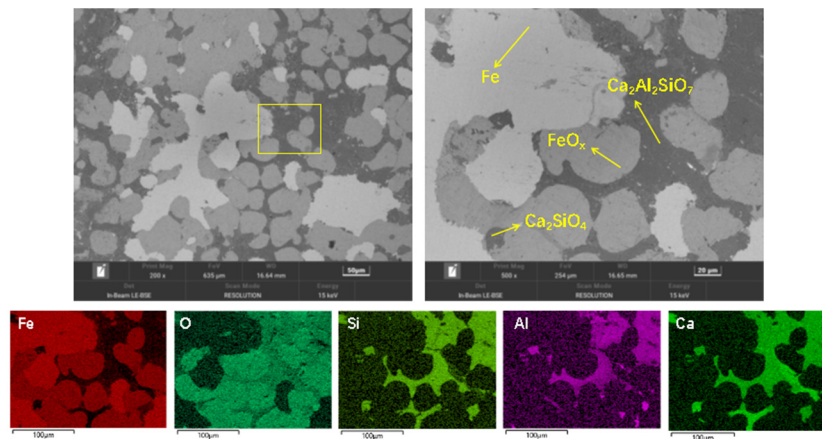


Figure 6. SEM-EDS analysis of internal deposit sample S2.

### 3.4. Iron Distribution Behavior in Deposits

The distribution patterns of iron in the main mineral phases of the deposits were analyzed by an Automatic Mineral Parameter Analyzer (MLA, Gemini Sigma 300, ZEISS, Oberkochen, Germany). MLA is one of the most advanced quantitative and automatic detection systems for process mineralogy in the world. It is based on the backscattered image data of samples collected by electron microscope, combined with the component identification function of an energy spectrum, forming the automatic identification and appraisal of minerals, and completing the automatic testing of minerals from morphology to composition. The micro-morphology and mineral phase distribution are shown in Figure 7.

Combined with the microscopic morphology results and the MLA color map analysis, it was found that the composition of the mineral phase in S1 and S2 was basically familiar, but their contents were different. Magnetite, iron-bearing silicate, and pure iron phases were clearly observed in S1, whereas a large amount of striated iron phase, some iron-bearing silicate phases, and a limited amount of magnetite were clearly observed in S2. No clear boundary between the iron-bearing silicate phase and iron phase in S1 and S2 was found. They were cemented to each other. The MLA analysis results might have combined the presence of FeO and Fe<sub>2</sub>O<sub>3</sub> into Fe<sub>3</sub>O<sub>4</sub> because the backscattered difference of FeO, Fe<sub>2</sub>O<sub>3</sub>, and Fe<sub>3</sub>O<sub>4</sub> were not significant enough.

Table 2 shows the content distribution of Fe in typical deposits. The main mineral phases in the S1 were magnetite (42.21%), iron-bearing silicate (27.49%), and pure iron (17.6%). Iron was mainly found in magnetite (48.35%), iron-bearing silicate (31.49%), and pure iron (20.16%). The main mineral phases in the S2 were iron-bearing silicate

(21.20%), iron phase (64.48%), and a small amount of magnetite (3.99%). Iron was mainly found in iron-bearing silicate (23.64%), the iron phase (71.91%), and magnetite (4.45%). By comparison, it was found that the significant differences in the composition of the S1 and S2 were contents of magnetite and iron phases. From S1 to S2, magnetite was essentially reduced to monomeric iron.

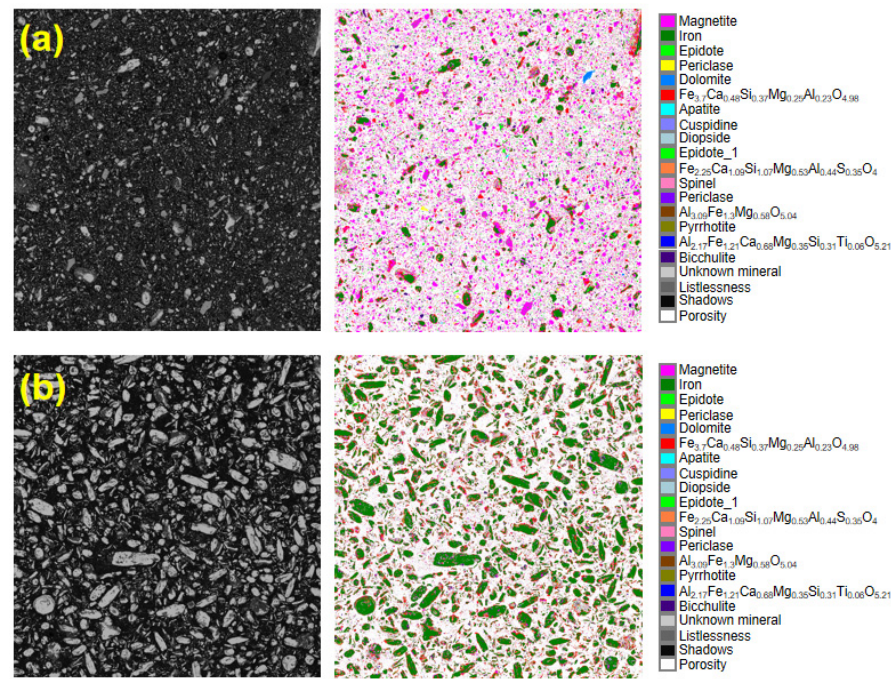


Figure 7. MLA diagram of typical deposits (a) S1; (b) S2.

The presence of fine particles in the raw material provided favorable conditions for deposit formation. With the rotation of the kiln, the ore particles slid and rolled in the kiln under the action of friction between the material and the kiln wall [39]. The raw material moved from the moving layer on the surface into the rising layer on the lower part. As seen in the above characterizations regarding the deposits, the iron in the steel dust sludge was over-reduced by carbon to form ferrous oxide, probably because the local temperature was too high. A large amount of iron oxides in the deposits existed in the form of FeO. As known, hematite begins to form ferrous oxide at about 900 °C under a certain reducing condition. Ferrous oxide can react with silica to form a eutectic liquid phase with a low melting point and silicate melt [40]. Thus, ferrous oxide plays a very important role in the generation of the low melting point eutectic liquid phase of deposit materials. In addition, the results of the phase analyses indicate that silicates are important phase components and binder phases in the deposits. These may be two of the important reasons for the formation and attachment of deposits to the kiln wall.

Table 2. Content distribution of iron in typical deposits.

Mineral	S1		S2		
	No.	Wt.%	Fe	Wt.%	Fe
Low count rate		0.02	0	0.02	0
Perovskite		0.03	0	0.15	0
Spinel		0.05	0	0.06	0
Iron-bearing silicate		27.49	31.49	21.20	23.64
Cuspidine		0.12	0	0.32	0
Dolomite		0.13	0	0	0
Periclase		0.17	0	0	0

Table 2. Cont.

Mineral	S1		S2		
	No.	Wt.%	Fe	Wt.%	Fe
Apatite		0.21	0	0.01	0
Pyrrhotite		0.44	0	0.15	0
Diopside		1.16	0	0.09	0
Bicchulite		3.24	0	2.22	0
Unknown mineral		7.13	0	7.31	0
Iron		17.6	20.16	64.48	71.91
Magnetite		42.21	48.35	3.99	4.45
Pore space (area ratio)			2.13		1.57

### 3.5. Mechanism for Deposit Formation

#### 3.5.1. Determination of the Main Control Phase

The above comprehensive analysis shows that silicates and iron oxides are two of the most important constituent phases in deposit formation. In order to determine the main control phases, purified material experiments were carried out to simulate the formation process of deposit components.

In the experiment,  $\text{SiO}_2$ ,  $\text{CaO}$ , and  $\text{Al}_2\text{O}_3$  were mixed according to the weight ratio of the deposit material ( $\text{SiO}_2:\text{CaO}:\text{Al}_2\text{O}_3 = 10.19:18.44:7.34$ ) and then divided into two groups A and B. Group A was directly roasted under a nitrogen atmosphere at  $1200^\circ\text{C}$  for 1 h, and group B was proportionally added with  $\text{Fe}_2\text{O}_3$  (61.6%) and then roasted under the same conditions. After quenching, the samples were ground for analysis. The results are shown in Figure 8 and they illustrate that the group A sample remained as powder, while the group B sample had melted and then solidified. This suggests that it was the iron-containing system, rather than the  $\text{Al}_2\text{O}_3\text{-SiO}_2\text{-CaO}$  system, that primarily affected the deposit formation. The XRD analysis results shown in Figure 9 illustrate that the main phase after roasting in group A was calcium silicate, while in group B calcium–aluminum yellow feldspar, a low melting point phase, appeared after roasting.

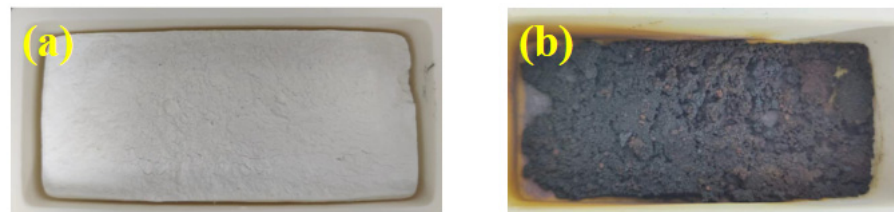
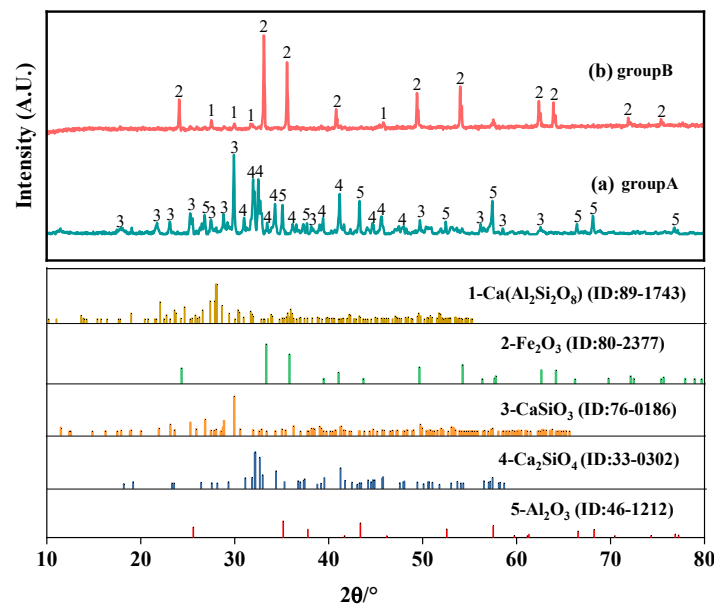


Figure 8. Physical picture of the samples (a)  $\text{SiO}_2\text{-CaO-Al}_2\text{O}_3$  and (b)  $\text{SiO}_2\text{-CaO-Al}_2\text{O}_3\text{-Fe}_2\text{O}_3$  after roasting.

In order to explore the process of phase change with temperatures, the purified materials were used to simulate the formation of deposit phases at different temperatures ( $900^\circ\text{C}$ ,  $1000^\circ\text{C}$ ,  $1100^\circ\text{C}$ ,  $1150^\circ\text{C}$ , and  $1200^\circ\text{C}$ ), and the baked samples were processed for XRD analysis. The results are shown in Figure 10.

As seen from the Figure, in the early stage of  $900^\circ\text{C}$  reduction, obvious  $\text{Fe}_3\text{O}_4$  and  $\text{FeO}$  diffraction peaks were detected. The  $\text{CaO}$  combined with  $\text{Fe}_2\text{O}_3$  to form ferrite  $\text{Ca}_2\text{Fe}_2\text{O}_5$ , and  $\text{CaO}$  further reacted with  $\text{SiO}_2$  to form  $\text{Ca}_2(\text{SiO}_4)$ . As the temperature increased, the reduction reactions continuously occurred. Due to the good solid solution of  $\text{Ca}_2(\text{SiO}_4)$ ,  $\text{FeO}$  dissolved in it and produced a complex iron-containing compound, calcium–iron pyroxene ( $\text{Ca}_{1.56}\text{Fe}_{1.44}\text{Fe}_2\text{SiO}_4$ ).  $\text{Ca}_2\text{Fe}_2\text{O}_5$  existed in the form of an intermediate product and gradually formed calcium iron pyroxene as the temperature increases. When the reduction reaction continued to  $1150^\circ\text{C}$ , the  $\text{Ca}_{1.56}\text{Fe}_{1.44}\text{Fe}_2\text{SiO}_4$  was gradually replaced by  $\text{Ca}_2\text{Al}(\text{AlSi})\text{O}_7$ . As the temperature continued to rise,  $\text{FeO}$  was further reduced to metal Fe particles, and  $\text{Ca}_2\text{Al}(\text{AlSi})\text{O}_7$  became the main phase with a relatively low melting point.



**Figure 9.** X-ray diffraction (XRD) patterns of the samples (a) SiO<sub>2</sub>-CaO-Al<sub>2</sub>O<sub>3</sub> and (b) SiO<sub>2</sub>-CaO-Al<sub>2</sub>O<sub>3</sub>-Fe<sub>2</sub>O<sub>3</sub> after roasting.

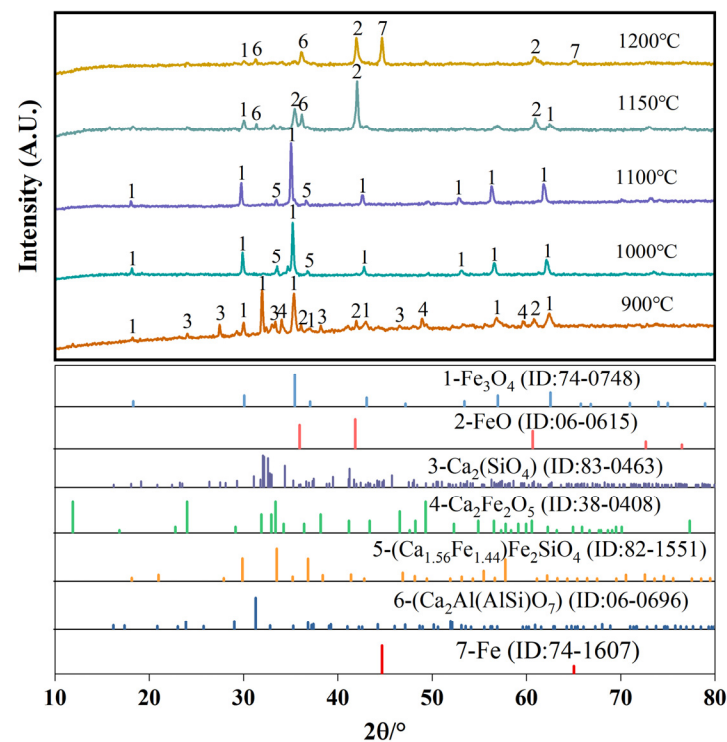


**Figure 10.** XRD patterns of the samples at different reduction temperatures.

The above results verify that the formation of the deposit phase during reduction was the result of the joint participation of the reducing product of iron oxide and alkaline oxide. And with the advancement of the reduction reaction, the complex iron-containing compounds were gradually replaced by calcium-containing compounds, and finally formed by deposits. Silicate plays an important role in knot coil formation, and its influence can be considered from several aspects. The type and content of silicates can affect the chemical composition and stability of the deposit; the presence of silicates can also affect the morphology and structure of the deposit.

### 3.5.2. Effects of FeO on the Liquid Phase in the Al<sub>2</sub>O<sub>3</sub>-SiO<sub>2</sub>-CaO-FeO System

The above results validate that iron oxide plays an important role in deposit formation. Considering that the FeO content changes during the reduction process, the thermodynamic calculation for the liquid phase of the CaO-Al<sub>2</sub>O<sub>3</sub>-SiO<sub>2</sub> basic slag system was carried out using FactSage<sup>®</sup> 8.1 software, and the effects of FeO content and atmosphere changes on the liquid phase region of CaO-Al<sub>2</sub>O<sub>3</sub>-SiO<sub>2</sub> system were investigated. The results are shown in Figure 11.

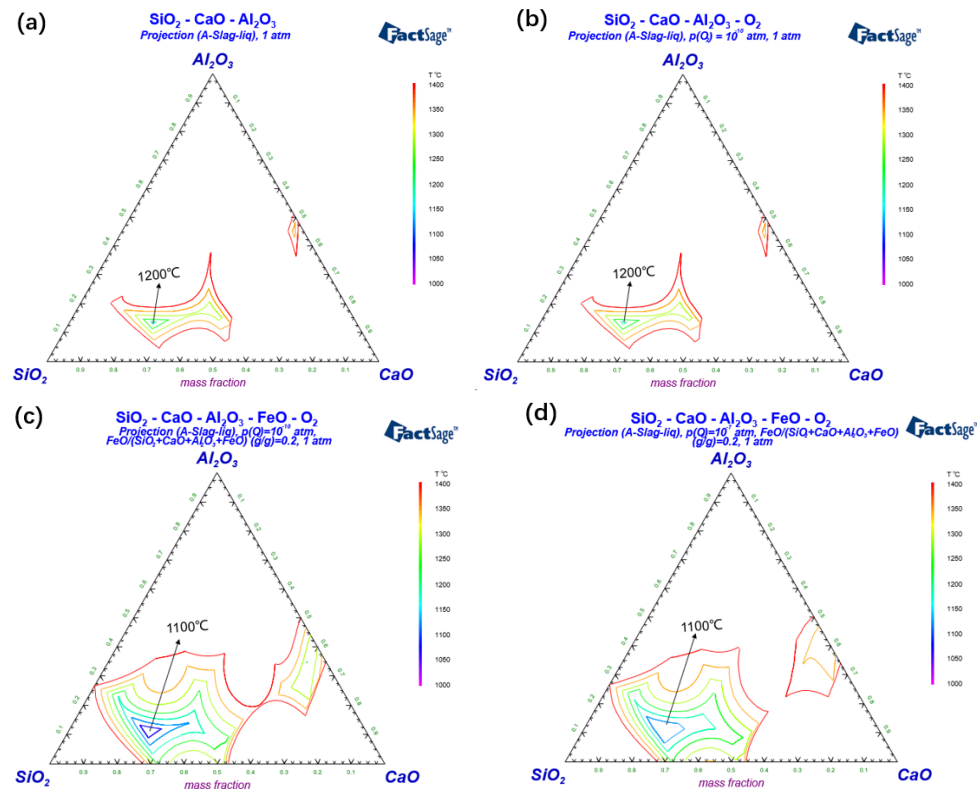


**Figure 11.** Effects on liquid areas of Al<sub>2</sub>O<sub>3</sub>-SiO<sub>2</sub>-CaO-FeO phase diagrams by FeO: (a) the Al<sub>2</sub>O<sub>3</sub>-SiO<sub>2</sub>-CaO system; (b) the Al<sub>2</sub>O<sub>3</sub>-SiO<sub>2</sub>-CaO system under p(O<sub>2</sub>) = 10<sup>-10</sup> atm; (c) the Al<sub>2</sub>O<sub>3</sub>-SiO<sub>2</sub>-CaO-FeO system under p(O<sub>2</sub>) = 10<sup>-10</sup> atm; (d) the Al<sub>2</sub>O<sub>3</sub>-SiO<sub>2</sub>-CaO-FeO system under p(O<sub>2</sub>) = 10<sup>-7</sup> atm.

Figure 11a,b shows the liquid phase region of the Al<sub>2</sub>O<sub>3</sub>-SiO<sub>2</sub>-CaO system as a function of temperature for different atmosphere conditions, respectively. Figure 11c,d demonstrates the variation of the liquid phase region with temperature after the addition of 20% FeO. The gap between adjacent isotherms in Figure 11 is 50 °C. Comparison of Figure 11b,c reveals that the liquid temperature decreased from 1200 °C to below 1100 °C after the addition of FeO. In Figure 11c, when ferrous oxide was added up to 20%, the 1100 °C liquid appeared at a region of 58~64% Al<sub>2</sub>O<sub>3</sub>, 6~10% CaO, and 16~22% SiO<sub>2</sub>. The comparison of Figure 11c,d also shows that the lower the oxygen partial pressure was, the lower the liquid temperature and the larger the liquid phase region area would be. The reason may be that the reduction produced more FeO. This study confirms the importance of FeO content for the formation of the liquid phase in the initial deposit [41]. FeO promotes the generation of liquid slag, which in turn promotes the migration and rearrangement of the phases. This results in the formation of deposits [42].

### 3.5.3. Liquid Formation Process in the FeO-Fe<sub>3</sub>O<sub>4</sub> and Fe-FeO System

The results in Section 3.5.2 indicate that ferrous oxide plays a very important role in the formation of low melting point eutectic liquid. In this section, FactSage<sup>®</sup> 8.1 software was used to draw the Fe-FeO and FeO-Fe<sub>3</sub>O<sub>4</sub> binary phase diagrams. We tried to verify the

formation mechanism of the deposit phase among iron components in the inner and outer deposit layer, and to analyze the melting point change in the mixed system.

As seen from Figure 12a, the Fe<sub>3</sub>O<sub>4</sub> and FeO system started to melt at around 1366 °C, where it could completely melt at FeO:Fe<sub>3</sub>O<sub>4</sub> = 0.87:0.13 (g/g). However, when the proportion of Fe<sub>3</sub>O<sub>4</sub> was too high, the melting temperature became high. Slag-liq regions expanded when the temperature exceeded 1366 °C. Figure 12b shows that the liquid phase could also be formed in the FeO-Fe system at 1366 °C, but only the crystalline transformation (Fe(s2)→Fe) and melting of metal Fe occurred with the increase in temperature.

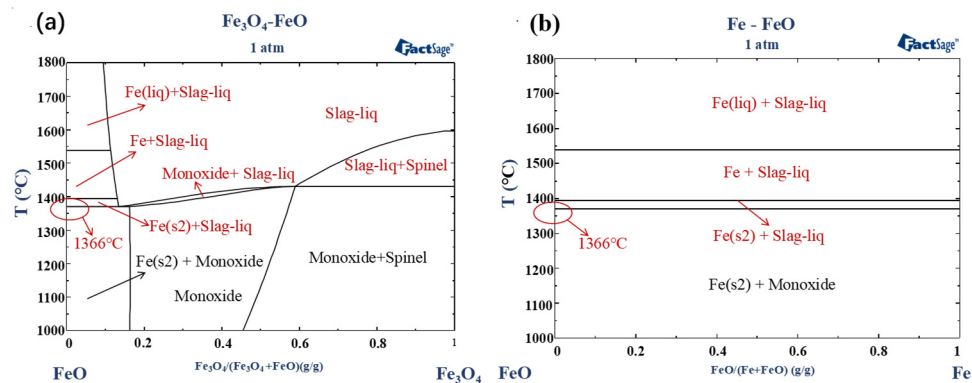


Figure 12. (a) FeO-Fe<sub>3</sub>O<sub>4</sub> binary phase diagram, (b) Fe-FeO binary phase diagram.

Combined with the analysis of the microstructure and the composition of deposits, the results indicate that the initial formation of the deposits may be mainly based on Fe<sub>3</sub>O<sub>4</sub>. With the continuous reduction of Fe<sub>3</sub>O<sub>4</sub> to FeO, a binary mixed system between Fe<sub>3</sub>O<sub>4</sub>-FeO formed. The melting point decreased, and the first liquid phase appeared and accumulated. With the continuous reduction of Fe<sub>3</sub>O<sub>4</sub> to Fe, the Fe<sub>3</sub>O<sub>4</sub>-FeO-Fe mixed system immediately formed, and the liquid region continued to expand. The above thermodynamic results illustrate that the liquid phase could also generate among iron components if the local temperature reached somewhere around 1366 °C.

### 3.5.4. Experimental Verification of the Fe<sub>3</sub>O<sub>4</sub>-FeO-Fe System

To verify the above results, samples of the FeO-Fe<sub>3</sub>O<sub>4</sub> and FeO-Fe systems were respectively prepared with pure analytical reagents. TG-DSC analysis was performed, and the results are shown in Figure 13.

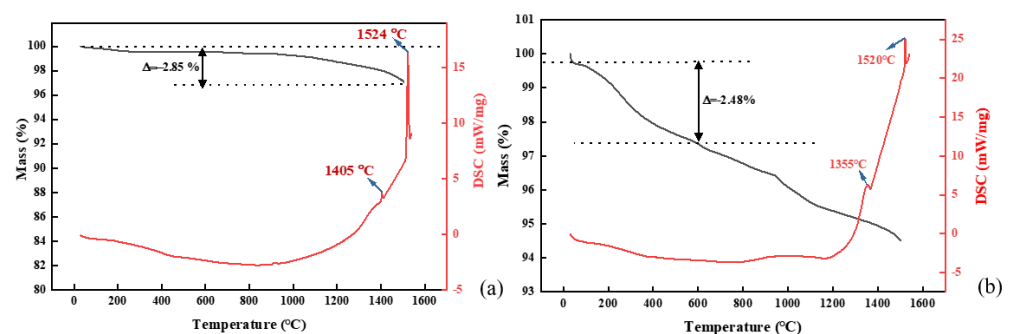
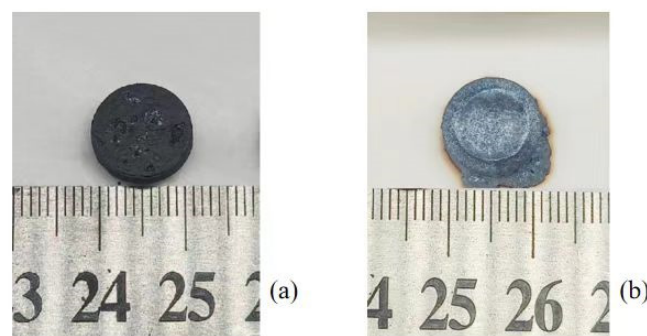


Figure 13. TG-DSC of the (a) FeO-Fe<sub>3</sub>O<sub>4</sub> and (b) Fe-FeO samples.

It can be seen from Figure 13 that the weight loss rate of the FeO-Fe<sub>3</sub>O<sub>4</sub> and Fe-FeO systems were 2.85% and 2.48%, respectively. The first exothermic peak of mixed FeO and Fe<sub>3</sub>O<sub>4</sub> in Figure 13a appeared at a low temperature, ranging roughly from 1405 °C, associating with the formation of a FeO-Fe<sub>3</sub>O<sub>4</sub> binary liquid. The second exothermic peak in 1524 °C corresponded to the melting of Fe<sub>3</sub>O<sub>4</sub>. Two exothermic peaks of the mixed Fe-FeO were detected roughly at 1355 °C and 1520 °C. Combined with the physicochemical properties of Fe

and FeO and Figure 12b, it is inferred that the first exothermic peak probably corresponded to the formation of the liquid phase in the system, while the second exothermic peak was due to the melting of Fe. The above results are in agreement with the thermodynamic analysis results. In the rotary kiln, the presence of FeO and Fe formed a liquid phase. Then, it further caused the deposit formation when the temperature decreased.

In addition, in order to more visually verify the melting process, liquid phase formation, and liquid composition of the above two systems at the aforementioned temperatures, two pure reagent systems of FeO-Fe<sub>3</sub>O<sub>4</sub> and Fe-FeO were prepared, respectively. Each sample was mixed evenly, pressed into a 10mm tablet, and then placed in an alumina crucible. We put the crucible into the vertical furnace with nitrogen atmosphere. The temperature was raised to 1450 °C for 15min, and then decreased to 1366 °C to equilibrium for 2h. The samples were immediately quenched and cooled with liquid nitrogen after the required holding time. Figure 14 shows the physical picture of samples.



**Figure 14.** The physical picture after roasting: (a) the mixed FeO-Fe<sub>3</sub>O<sub>4</sub> system, (b) the mixed Fe-FeO system.

As seen from Figure 14, after roasting, the main body of the mixed FeO-Fe<sub>3</sub>O<sub>4</sub> sample still remained a solid tablet. After roasting, the texture was hard, but no obvious liquid phase was formed. However, the mixed FeO-Fe presented a melting phenomenon, and a clear liquid phase was visible around its perimeter.

### 3.5.5. Experimental Verification of Raw Material Deposits

The actual factory raw materials were used to validate the knot formation under an extreme condition, which simulated the locally high-temperature environment in the rotary kiln. The composition of mixture is presented in Table 3. The investigations were performed under 1366 °C to observe whether the liquid phase was formed. The experimental results are shown in Figure 15. As shown in the Figure, the actual mixed dust and mud raw materials melted into liquid at 1366 °C, and flowed flatly inside the corundum boat.

**Table 3.** The composition of mixture (g).

ZnO	Fe <sub>2</sub> O <sub>3</sub>	CaO	SiO <sub>2</sub>	Al <sub>2</sub> O <sub>3</sub>
16.50	47.39	7.22	1.54	0.68

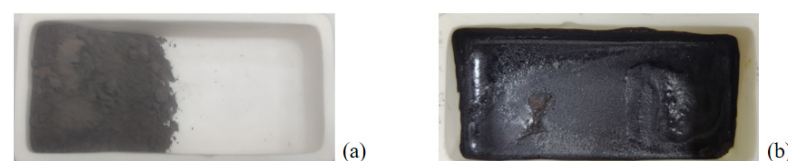


**Figure 15.** The picture of steelmaking dust raw materials: (a) before roasting, (b) after roasting.

Figure 16 shows the SEM mapping of roasting products. It illustrates that iron was mainly concentrated in the white liquid region. A small amount of iron was presented in the

iron oxide particle. The liquid approximately comprised iron oxides. Silicon and calcium tended to combine together in the strip liquid area and surround the iron components. Part of the calcium existed in the individual calcium oxide particles. Almost all silicon combined with calcium in the strip liquid area. This indicates that, in the reduction roasting process, if the local temperature were high enough, both iron oxides and calcium silicate were able to lead to ring formation.

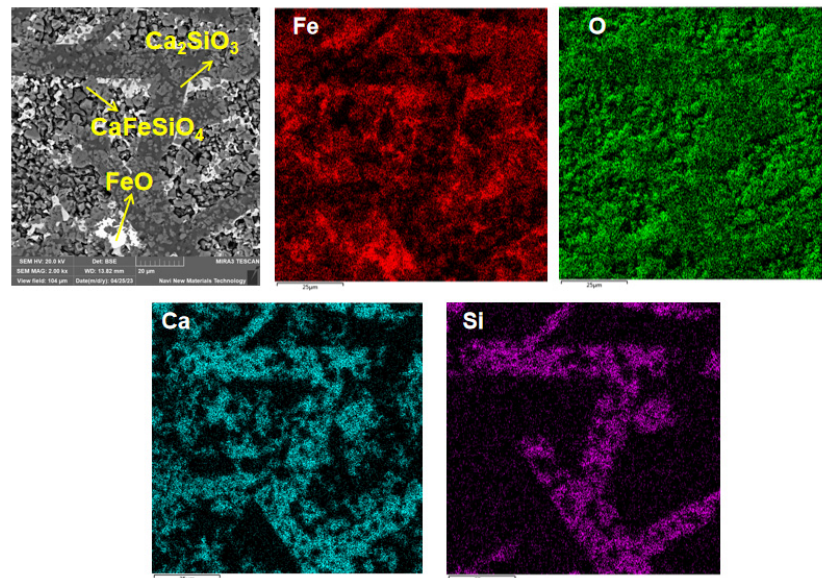


Figure 16. EDS element mapping of roasted actual factory raw materials.

Based on the above investigations, a schematic diagram of the rotary kiln ring formation mechanism was drawn and shown in Figure 17. After the steelmaking dust was fed into the rotary kiln, it ran along with the rotation dip angle of the furnace body. In the initial stage, alkaline components, such as CaO, reacted with SiO<sub>2</sub> to form Ca<sub>2</sub>SiO<sub>4</sub> with good solid solubility. In addition, Fe<sub>2</sub>O<sub>3</sub> is reduced to Fe<sub>3</sub>O<sub>4</sub>. In the high temperature melting zone, Fe<sub>3</sub>O<sub>4</sub> was reduced to FeO to form the Fe<sub>3</sub>O<sub>4</sub>-FeO system, and initial liquid phase condensation occurred. Part of FeO dissolved in Ca<sub>2</sub>SiO<sub>4</sub> to form CaFeSiO<sub>4</sub>, which was the intermediate phase in the formation of deposits. As the ambient temperature and reducing atmosphere continued to act, deposits accumulated. Then, iron oxides continue to be reduced to Fe, forming a Fe<sub>3</sub>O<sub>4</sub>-FeO-Fe mixed system. On the other hand, Ca<sub>2</sub>Al<sub>2</sub>SiO<sub>7</sub>, with a relatively low melting point gradually became the main complex phase. The liquid phase of the deposit formation increased, and became dense and hard.

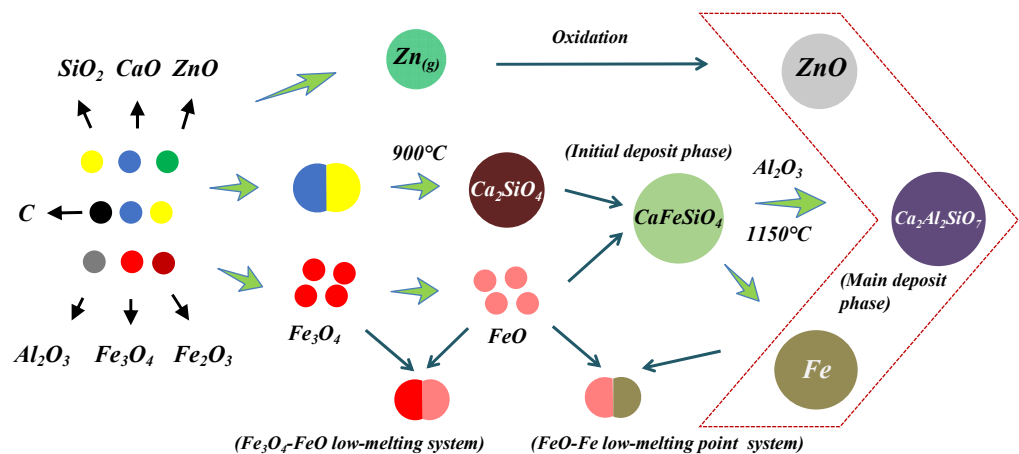


Figure 17. Schematic diagram of the oxide reduction and formation mechanism of the deposit.

#### 4. Conclusions

In the process of steelmaking dust treatment in the rotary kiln, deposit formation can lead to channel blockage and reduce the processing capacity. In severe cases, the operation has to be stopped and the device is damaged. This study reveals the formation and growth mechanism of the deposit by testing and analyzing samples collected from actual deposits. The mineral characteristic results show that the mineral composition of the deposits was magnetite, monolithic iron, olivine, and yellow feldspar. In the deposit, a clear metallic luster (iron grey) deposit material and many molten substances connected to a piece. The phase compositions of the inner and outer deposit were different. The outer deposition contained more iron and less ferrous oxide. This phenomenon may be caused by a different reducing environment. For the internal deposit closed to the refractory brick, the reduction of iron oxides took place in the initial reaction period, and would be covered by the newly formed deposit, which stopped the further reduction of iron oxides.

The thermodynamic calculations and experimental investigation results show that the formation process of deposits was accompanied by the participation of alkaline oxides and iron oxides. The intermediate product  $\text{Ca}_2\text{SiO}_4$  can promote the generation of low melting point phases, such as  $\text{CaFeSiO}_4$ , and  $\text{Ca}_2\text{Al}_2\text{SiO}_7$ . Iron oxides play an important role in deposit formation. The reduction intermediate product FeO facilitated the generation of liquid ferrous mixture ( $\text{Fe}_3\text{O}_4$ -FeO and  $\text{Fe}_3\text{O}_4$ -FeO-Fe mixture), which in turn further promoted the growth of the initial deposit phase. The solid deposit formed and attached to the kiln inner wall, along with a decrease in temperature.

**Author Contributions:** X.M.: supervision, conceptualization, and review; L.H.: investigation, validation, original draft preparation, and writing and editing; M.Y.: data curation and software; Y.W., Y.K. and C.P.: suggestion and review; X.Y.: project administration and suggestion; Q.H.: methodology and data curation; Y.L.: conceptualization, methodology, project administration, supervision, writing and editing, review, and confirmation. All authors have read and agreed to the published version of the manuscript.

**Funding:** This research was funded by National Key R&D Program of China (2022YFC3901603), National Natural Science Foundation of China (52104356), the financial support from the Science and Technology Innovation Program of Hunan Province (2023RC3059), Foundation for Innovative Research Groups of the National Natural Science Foundation of China (52121004), The Science and Technology Innovation Program of Hunan Province (2021RC3013), and Science and Technology Project of Gansu Province (21ZD4GD033), Fundamental Research Funds for the Central Universities of Central South University (2024zzts010).

**Data Availability Statement:** Data are contained within the article.

**Acknowledgments:** The authors thank Zhongye Changtian International Engineering Co., Ltd. for supplying the experimental deposit materials. The authors gratefully acknowledge support from Central South University.

**Conflicts of Interest:** The authors declare no conflicts of interest.

#### References

1. Chai, L.; Shi, M.; Liang, Y. Behavior, distribution and environmental influence of arsenic in a typical lead smelter. *J. Cent. South Univ.* **2015**, *22*, 1276–1286. [[CrossRef](#)]
2. Shang, H.; Li, H.; Wei, R.; Long, H.; Li, K.; Liu, W. Present situation and prospect of iron and steel dust and sludge utilization technology. *Iron Steel* **2019**, *54*, 9–17.
3. Peng, B.; Song, H.; Chai, L.; Wang, J.; Wang, Y.; Min, X.; He, D. Reduction mechanism of stainless steelmaking dust and carbon pellets. *Trans. Nonferrous Met. Soc. China* **2005**, *15*, 1407–1413.
4. Liu, L.; Zhao, Q.; Feng, X. Study on separation of zinc and iron from dust ash containing zinc. *J. Iron Steel Res.* **2020**, *32*, 714–719.
5. Zhang, J.; Li, Y.; Yuan, J.; Liu, Z. Present situation and prospect of dust treatment in Chinese iron and steel enterprises. *Iron Steel* **2018**, *53*, 6–15.
6. Lv, W.; Wang, L.; Zhang, H.; Li, Z.; Wang, L.; Li, F. Research on progress of zinc extraction process from iron and steel metallurgical sludge. *Iron Steel* **2023**, *59*, 157–167.
7. Chen, W.; Yang, T.; Li, Q.; Li, Q.; Shi, Y.; Ye, M. Characteristic Analysis and Separation of Zinc and Iron from Zinc Containing Metallurgical Dust. *Non-Ferr. Met. (Smelt. Compon.)* **2023**, *09*, 126–136.

8. Yi, Z.; Xiao, H.; Song, J. Mathematic simulation of heat transfer and operating optimization in alumina rotary kiln. *J. Cent. South Univ.* **2013**, *20*, 2775–2780. [[CrossRef](#)]
9. Wang, D.; Hua, S.; Wu, L.; Liu, K.; Wang, H. Coupled Thermodynamics and Phase Diagram Analysis of Gas-Duct Concretion Formation in Pyro-Processing Ironmaking and Steelmaking Dust. *Minerals* **2021**, *11*, 1125. [[CrossRef](#)]
10. Eriksson, M.; Carlborg, M.; Brostrom, M. Characterization of Ring Deposits Inside a Quicklime Producing Long Rotary Kiln. *Energy Fuels* **2019**, *33*, 11731–11740. [[CrossRef](#)]
11. Zhao, J. Process analysis of Resource Utilization On Zinc-borne dust and sludge in iron and steel plant. *World Non-Ferr. Met.* **2018**, 272–274.
12. Zhao, J.; Zhang, Z.; Li, B.; Wei, X. Formation and Growth Behavior Analysis of Slagging Rings in Rotary Kiln-Type Hazardous Waste Incineration Systems. *Energies* **2021**, *14*, 561. [[CrossRef](#)]
13. Wang, Z.; Li, Y.; Tang, J.; Wang, J.; She, X.; Xue, Q.; Zuo, H. Status and progress of resource recovery and utilization of dust and sludge in the steel industry. *Jiangxi Metall.* **2023**, *43*, 87–94.
14. Zhu, D.; Qiu, G.; Jiang, T.; Xu, J. An Innovative Process for Direct Reduction of Cold bound Pellets from Iron Concentrate with a Coal-based Rotary Kiln. *J. Cent. South Univ. Technol. (Engl. Ed.)* **2000**, *2*, 68–71.
15. Guo, X. Current Status and Improving Direction of Rotary Kiln Technology for Treating Zinc-bearing Dust and Mud. *Ind. Heat.* **2023**, *52*, 41–44.
16. Wang, T. Analysis on Key Technology of Treating Steel Containing Zinc Dust in Rotary Kiln. *China Resour. Compr. Util.* **2019**, *37*, 181–184.
17. Lin, H.; Weng, W.; Zhong, S.; Qiu, G. Enhanced recovery of zinc and lead by slag composition optimization in rotary kiln. *Trans. Nonferrous Met. Soc. China* **2022**, *32*, 3110–3122. [[CrossRef](#)]
18. Wang, X.; Li, T.; Sun, X.; Zhang, J.; Liu, Z.; Wang, Y.; Ma, L. Study on the intrinsic relationship between pellet ore properties and mineral phases of rotary kiln nodules. *Energy Metall. Ind.* **2022**, *41*, 45–49.
19. Zhang, X.; Wang, M.; Feng, Z.; Chen, Z.; Li, S. Causes and prevention of ring formation in rotary kiln. *Refract. Lime* **2021**, *46*, 19–21.
20. Ding, C.; Liu, H.; Liu, S.; Zhao, H.; Ning, S. Analysis on Causes Leading to Circinate Conglutination of Kiln Burden in Metallurgical Rotary Kiln for Lime and Solution to Problem. *Angang Technol.* **2022**, *05*, 50–53.
21. Song, Y.; Zhao, C. Analysis and Preventive Measures of Ring-Forming in Metallurgical Lime Rotary Kiln. *ShanXi Metall.* **2021**, *44*, 239–240+245.
22. Liu, B.; Li, G.; Xie, W. Analysis and measures of ring formation in metallurgical lime rotary kiln. *Refract. Lime* **2020**, *02*, 009.
23. Ding, C.; Zhao, H.; Wang, Y. Causes and treatment methods of metallurgical lime rotary kiln ring formation. *Refract. Lime* **2022**, *47*, 39–41.
24. Shen, B.; Zhao, X. Analysis and prevention on ringing of lime rotary kiln with pulverized coal as fuel. *Refract. Lime* **2018**, *05*, 003.
25. Zhong, Q.; Yang, Y.; Jiang, T.; Li, Q.; Xu, B. Effect of coal ash on ring behavior of iron-ore pellet powder in kiln. *Powder Technol.* **2018**, *323*, 195–202. [[CrossRef](#)]
26. Qi, L.; Wang, B.; Ma, W.; Yang, Y.; Li, Q. Study on influences of firing coal quality on ringing of rotary kiln. *Sinter. Pelletizing* **2016**, *41*, 28–32.
27. Hou, E.; Wang, B.; Yang, Y.; Li, Q.; Zhong, Q.; Zhang, Y.; Quan, L. Influence of characteristics of coal on ring formation of rotary kiln. *Iron Steel Res.* **2016**, *44*, 9–13.
28. Luo, G.; Nie, X.; Wu, S.; Wang, Y.; Liu, J.; Zhou, S. Influence of F, K, Na on the ring formation properties of oxidized pellet rotary kiln. *Sinter. Pelletizing* **2013**, *3*, 29–32.
29. Zhong, R.; Yi, L.; Huang, Z.; Shen, X.; Jiang, T. Sticking mechanism of low grade iron ore-coal composite in rotary kiln reduction. *Powder Technol.* **2018**, *339*, 625–632. [[CrossRef](#)]
30. Si, J.; Jia, Y.; Liu, J.; Liang, D.; Hou, J. Structure of rings and ring forming mechanism of rotary pelletizing kiln. *Ironmak Steelmak* **2014**, *49*, 17–21.
31. Yang, X. Fundamental and Applied Studies on Preparing Oxidized Pellets from Mixed Iron Ore Concentrates. Ph.D. Thesis, Central South University, Changsha, China, 2011.
32. Fan, X.; Gan, M.; Yuan, L.; Li, G.; Jiang, T.; Zhuang, J. Study of Mechanism on Ring Formation in Grate-Kiln of Acid Pellet. *Iron Steel* **2008**, *43*, 6.
33. Nie, J.; Zhang, Z.; Qiao, W.; Sun, J.; Chen, J.; Zhou, Q.; Liang, Y. Characteristics of the pellet rotary kiln ring. *J. Wuhan Univ. Sci. Technol.* **2010**, *33*, 527–531.
34. Wang, Y.; Zhang, J.; Liu, Z. Rings growth behavior within a pre-reduction rotary kiln: The layered structure and formation mechanism. *Powder Technol.* **2019**, *356*, 73–82. [[CrossRef](#)]
35. Zhao, J.; Wei, X.-L. Behavior of alkali metals in fly ash during waste heat recovery for municipal solid waste incineration. *Energy Fuel* **2018**, *32*, 4417–4423. [[CrossRef](#)]
36. Zhu, H.-M.; Wang, Y.-F.; Jing, N.-J.; Jiang, X.-G.; Lv, G.-J.; Yan, J.-H. Study on the evolution and transformation of chlorine during co-processing of hazardous waste incineration residue in a cement kiln. *Waste Manag.* **2019**, *37*, 495–501. [[CrossRef](#)]
37. Wang, S.; Guo, Y.-F.; Fan, J.-J. Initial stage of deposit formation process in a coal fired grate-rotary kiln for iron ore pellet production. *Fuel Process. Technol.* **2018**, *175*, 54–63. [[CrossRef](#)]
38. Huffman Gerald, P.; Huggins Frank, E.; Dunmyre George, R. Investigation of the high-temperature behaviour of coal ash in reducing and oxidizing atmospheres. *Fuel* **1981**, *60*, 585–597. [[CrossRef](#)]

39. Li, S.-H.; Zhang, X.; Zhang, L.-D.; Yu, K.-S. Numerical simulation of particles axial mixing in rotary kiln. *China Powder Sci. Technol.* **2011**, *17*, 23–26. [[CrossRef](#)]
40. Zeng, T.; Helble Joseph, J.; Bool, L.E.; Sarofim Adel, F. Iron transformations during combustion of Pittsburgh no. 8 coal. *Fuel* **2009**, *88*, 566–572. [[CrossRef](#)]
41. Wang, S.; Guo, Y.-F.; Chen, F. Combustion reaction of pulverized coal on the deposit Formation in the kiln for iron ore pellet production. *Energy Fuels* **2016**, *30*, 6123–6131. [[CrossRef](#)]
42. He, H.-Y.; Hu, B.-P.; Ding, J. Relationship between slag behavior and consolidation strength of zinc-bearing dust pellets during direct reduction process. *J. Wuhan Univ. Sci. Technol.* **2023**, *46*, 241–246.

**Disclaimer/Publisher’s Note:** The statements, opinions and data contained in all publications are solely those of the individual author(s) and contributor(s) and not of MDPI and/or the editor(s). MDPI and/or the editor(s) disclaim responsibility for any injury to people or property resulting from any ideas, methods, instructions or products referred to in the content.